Ion Migration and Space-Charge Zones in Metal Halide Perovskites Through Short-Circuit Transient Current and Numerical Simulations

Agustin O. Alvarez, Marisé García-Batlle, Ferdinand Lédée, Eric Gros-Daillon, Javier Mayén Guillén, Jean-Marie Verilhac, Thibault Lemercier, Julien Zaccaro, Lluis F. Marsal, Osbel Almora, and Germà Garcia-Belmonte*

The inherent ion migration in metal halide perovskite materials is known to induce deleterious and highly unstable dark currents in X- and γ-ray detectors based on those compounds upon bias application. Dark current slow drift with time is identified as one of the major drawbacks for these devices to satisfy industrial requirements. Because dark current establishes the detectability limit, current evolution, and eventual growth may mask photocurrent signals produced by incoming X-ray photons. Relevant information for detector assessment is ion-related parameters such as ion concentration, ion mobility, and ionic space-charge zones that are eventually built near the outer contacts upon detector biasing. A combined experimental (simple measurement of dark current transients) and 1D numerical simulation method is followed here using single-crystal and microcrystalline millimeter-thick methylammonium-lead bromide that allows extracting ion mobility within the range of $\mu_{ion} \approx 10^{-7}$ cm^2 V^{-1} s^{-1}, while ion concentration values approximate $N_{ion} \approx 10^{15}$ cm^{-3}, depending on the perovskite crystallinity.

1. Introduction

Metal halide perovskite (HP) materials have been successfully used in emerging applications such as ionizing-radiation detectors,[1–3] fulfilling fast and efficient detection of hard X- and γ-ray with high energy resolution, which is critical in medical imaging, scientific research and industrial inspections.[4] Behind that HPs application, there is a large enough $\mu\tau$-product and strong stopping power of the incoming ionization photons.[5] However, these materials still face some limitations. Namely, the inherent ion migration in HPs compounds is believed to result in deleterious and highly unstable dark current (no incoming X-ray photons).[6] Moreover, dark current instability and slow charge carrier displacement over long-term poling have been identified among the major drawbacks for these compounds to satisfy industrial requirements.[7] Furthermore, dark current establishes the detectability limit,[8] so that ion-related field screening destabilizes carrier drift reducing sensitivity. Therefore, analysis of the long-term dark current response of perovskite-based thick X-ray detectors has focused widespread attention.[7]

A. O. Alvarez, M. García-Batlle, G. Garcia-Belmonte
Institute of Advanced Materials
Universitat Jaume I
Castelló 12071, Spain
E-mail: garciag@uji.es

A. O. Alvarez
Center for Nanophotonics
AMOLF
Science Park 104, Amsterdam 1098 XG, The Netherlands

M. García-Batlle
University of North Carolina at Chapel Hill
NC 27599, USA
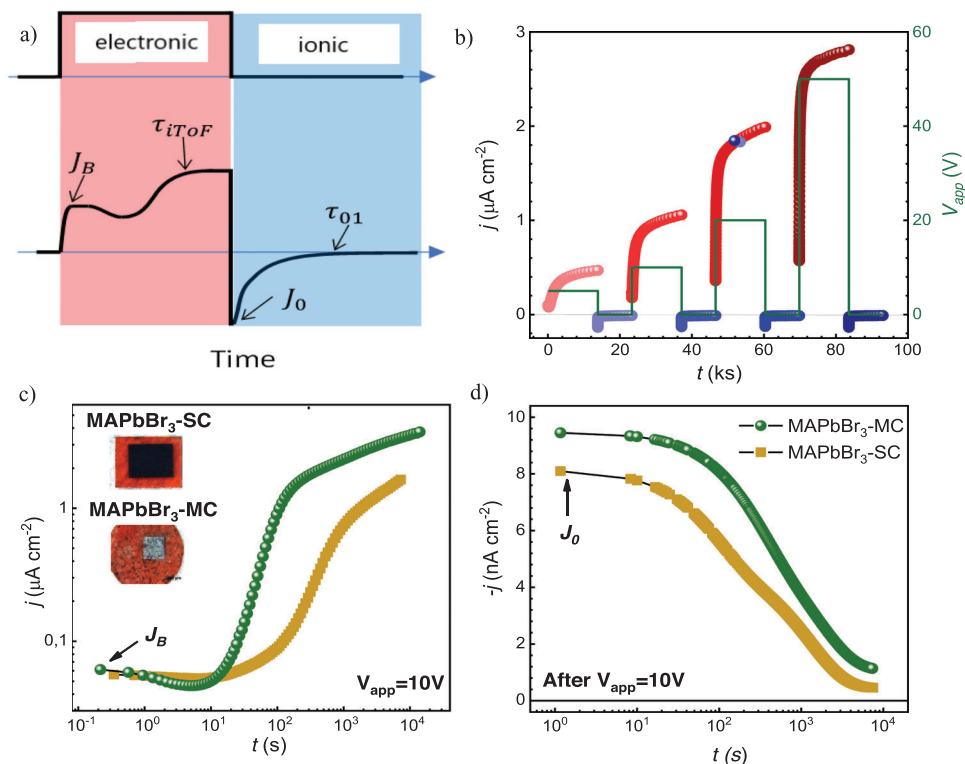
F. Lédée, E. Gros-Daillon, J. M. Guillén
Univ. Grenoble Alpes
CEA
Leti
F38000 Grenoble, France

J.-M. Verilhac
Univ. Grenoble Alpes
CEA
Liten
F38000 Grenoble, France

T. Lemercier, J. Zaccaro
Univ. Grenoble Alpes
CNRS Grenoble INP
Institut Néel
Grenoble F38042, France

L. F. Marsal, O. Almora
Department of Electronic
Electric and Automatic Engineering
Universitat Rovira i Virgili
Tarragona 43007, Spain

**ADVANCED
SCIENCE NEWS**

www.advancedsciencenews.com

**ADVANCED
ELECTRONIC
MATERIALS**

www.advelectronicmat.de

Figure 1. a) Schemed procedure of the experiment: A pulse of forward bias $V \neq 0$ V is applied during a long time until the dark current saturates. Then the short-circuit ($V = 0$ V) condition induces an ionic dark current in the opposite direction with long-term decay to equilibrium. Initial currents J_B and J_0, and characteristic times τ_{iToF} and τ_{01} are indicated. b) Example of the dark current evolution following the step voltage biasing protocol. Typical current response for ≈ 2 mm-thick MAPbBr$_3$ single crystal and ≈ 1.5 mm-thick MAPbBr$_3$-microcrystalline for c) long-term forward current response at 10 V applied bias, and d) recovery current at $V = 0$ V after previous 10 V polarization for single- and microcrystalline samples. Data in (b,c,d) are adapted under the terms of the CC-BY license.[9] Copyright 2022, The Authors. Published by American Chemical Society.

Previous works in the literature[9–11] have shown the evolution of dark current with time upon a step-voltage stimulus. This is shown in **Figure 1a**: during biasing (voltage step) the current increases in several stages before reaching the steady state, while after bias removal a small current undershoot appears. Figure 1b shows an example of the most common long-term electrical response in the case of thick perovskite layers following an on/off protocol with increasing bias, observed either for single crystals or microcrystalline films. It has been reported that the current reaches an initial value J_B (Figure 1c) and then slightly decrease at short times upon bias application (in the 1–100 s timescales). Subsequently, the current tends to increase by orders of magnitude with a much longer characteristic stabilization time τ_{iToF} ($10–10^4$ s, depending on the applied voltage). Since ions cannot establish a DC current, it is assumed that the steady-state, saturation current is exclusively originated by the flow of electronic carriers.[6] Also dark current at $t > 100$ s is dominated by the electronic currents, which are modulated by the less significant ionic current in a sort of ionic-electronic coupling in which ion kinetics effectively state the electronic current level.[9] Most likely, a reduction of contact electronic barriers via electrode polarization caused by ion accumulation fosters electronic carrier injection. However, large contributions of ionic current to the initial J_B are not discarded, as deduced from simulation analyses.[12] When bias is removed ($V = 0$ V), the registered dark current differs both in value and sign in comparison with that observed upon biasing ($V \neq 0$ V), with characteristic values of initial recovery current J_0 and relaxation time τ_{01} (see Figure 1d for experimental examples). One might propose the occurrence of exclusively displacement currents behind the observed current undershoot. However, by using simulation tools we observed that displacement currents only significantly contribute at shorter times, being ionic currents dominant at much longer times (see Results Section). A simpler explanation connects the relaxation currents at $V = 0$ V (after bias removing) to the rearrangement of mobile ions previously forming space-charge zones in the vicinity of the contacts.

As noted, mobile ions have been found behind the kinetics of such a featured electrical response.[6,13] In principle, ion migration in the long-term time range (from seconds to hours) is expected to be driven either by the electric field drift or ion diffusion depending on the position within the semiconductor layer. Although it is assumed that current transients must contain crucial information concerning mobile ion mobility and concentration, direct extraction of these ionic-related electrical parameters from the different biasing steps is by now only partially or not completely understood. However, it is considered an important piece of knowledge for the HP X-ray detector assessment and certainly for other perovskite-based technologies such as solar cells, photodetectors, and memristors.

ADVANCED
SCIENCE NEWS

www.advancedsciencenews.com

**ADVANCED
ELECTRONIC
MATERIALS**

www.advelectronicmat.de

In this work, we review the latest progress on the connection of dark current transient signals and ionic parameters as migrating ion concentration and ionic mobility. Attention is focused here on the analysis of zero-bias current recovery (current undershoot) after previous long-term polarization using new measurements. Although a current undershoot is also observed in semiconductor devices with negligible ion migration (Si or GaAs) after poling, much faster responses are expected in the range of µs–ms, in opposition to the measured decays as long as 10^4 s in our experiments. Moreover, that experimental procedure is adopted because electronic current components at $V = 0$ V should rapidly vanish, in the timescale of the dielectric relaxation time $\tau_d = R\,C_g$, being R the sample resistance (see Figure S3b, Supporting Information, and Experimental Section) and C_g the geometrical capacitance (Figure S3c, Supporting Information). Our samples exhibited values for $\tau_d \approx 100$ µs, leaving the long-term ($t > 10$ s) current decay exclusively determined by the mobile ion rearrangement, simplifying, therefore, our analysis. Note that this is not the case when $V \neq 0$ V as electronic current effectively establishes the registered levels for longer times, several orders larger than ionic currents.[6] By comparing experimental electrical responses of single-crystal and microcrystalline millimeter-thick methylammonium-lead bromide (MAPbBr$_3$), mobile ion concentration and mobility values were extracted. The analysis is complemented with the use of numerical simulation tools mimicking the structure and morphology of the detectors with the open-source MATLAB's code Driftfusion.[14] Ion mobility is observed to be within the range of $\mu_{ion} \approx 10^{-7}$–$10^{-6}$ cm^2 V^{-1} s^{-1}. It is already known by transient capacitance ion drift that MA-related defect migration in MAPbBr$_3$ is largely suppressed, while it is observed for MAPbI$_3$.[15] This fact moves us to regard bromide vacancies V_{Br}^+ as the cationic mobile ionic species causing the observed current transient. Ion mobility in lead perovskites within the range of 10^{-6} cm^2 V^{-1} s^{-1} was previously encountered self-consistently through current transients and impedance spectra.[16–19] It is also noticeable that similar values have been reported for anion vacancy mobility in the case of CsPbBr$_3$ by means of density functional theory calculations as a function of pressure.[20–21] In our analysis equilibrium ion concentration approximate $N_{ion} \approx 10^{15}$ cm^{-3}, depending on the perovskite crystallinity, in the lower range of values usually reported.[22]

2. Results and Discussion

At zero-voltage conditions (Figure 1d), individual current contributions of both electronic (originated by electrons J_n and holes J_p) and ionic (cations J_c and anions J_a) origin should be considered. For each kind of charge carrier, the driving force for charge migration can be either the electrical field (drift) or density gradients (diffusion). In addition, displacement current $J_{disp} = \epsilon_0\,\epsilon_r\partial\xi/\partial t$ (being ϵ_0 the vacuum permittivity, ϵ_r the dielectric constant, and ξ the local electrical field) is also expected in any transient experiment. There exists then a complex scenario to elucidate dominant current contributions, which may be also position-dependent. To illustrate the ionic parameter influence on the current recovery at $V = 0$ V, a series of numerical simulations were performed. 1D drift-diffusion simulation tools are a common approach among perovskite photovoltaic cells,[14,23–25] and similar formalisms have been explored for X-ray detectors.[12,26] In our case, the simula-

tion of dark current versus time follows the same assumptions as our previous works[12,27] at short circuit, i.e., pre-biasing for a long enough time in order to reach the current steady state. An illustrative example of the different contributions to total current is shown in Figure S5 (Supporting Information). Restricting our analysis to long-term ($t > 10$ s) features, one can observe that cation current dominates over other non-negligible contributions, particularly $J_c \gg J_p, J_{disp}$. The anion current is suppressed, $J_a = 0$, in our simulations. This result reinforces our initial assumption about the ionic origin of the recovery current at longer times.

Two main parameters are extracted from transient experiments: J_0 and τ_{01} (as indicated in Figure 1a). An initial ionic short-circuit current follows the ohmic-like behavior as.[27]

$$J_0 = q\mu_{ion}N_{ion}\frac{V_{pre}}{L} \tag{1}$$

where L is the sample thickness and V_{pre} is the remnant voltage just after the short-circuit ($V = 0$ V) is applied,[28] whose value depends on the shielding caused by the build-in space-charge ionic zones in the vicinity of the outer contacts (see below).[29–30] Note that initially $V_{pre} = -V$. This parameterization informs that in the initial recovering times ($t > 10$ s) mobile ions feel the internal electric field build during the polarization period, which effectively screens the external bias within the perovskite bulk region for high enough N_{ion} values.[27] The drift-controlled stage is corroborated in Figure S6 (Supporting Information) in which drift and diffusion components of J_c are plotted. As deduced from simulations, the drift component equals the cation current at any bulk position within the device ($x = L/2$ is chosen as a representative point). It is otherwise expected that the ionic movement rearrangement should proceed by diffusion in zones of huge concentration gradients (particularly in the accumulation space-charge zone at the negative electrode $x = L$, see final discussion on the spatially-varying ion cncentration) with a characteristic time τ_{01}, which can be defined when the current absolute value is reduced to 1% of the initial value, i.e., a decrease of the 99%. The occurrence of the long-term diffusion-controlled trends is in agreement with the bias-independent response time resulting from previous simulations.[12,27] There we also observed the interesting dependence $\tau_{01} \propto N_{ion}^{-1/2}$, which relates to the classical equation for the diffusion time $\tau = LL_D/D_{ion}$,[31] being $L_D = (\epsilon_0\epsilon_r k_B T/q^2 N_{ion})^{1/2}$ the ion Debye length, D_{ion} the ionic diffusivity, T is the temperature, and k_B the Boltzmann constant. Using the Einstein's relation, an expression for τ_{01} in terms of the main material parameters results as.[27]

$$\tau_{01} = \frac{\varsigma L}{\mu_{ion}}\sqrt{\frac{\epsilon_0\epsilon_r}{N_{ion}k_B T}} \tag{2}$$

where $\varsigma \approx 4.6$ is a dimensionless coefficient introduced in the parameterization of τ_{01}. Large diffusion cation current is corroborated by simulation in Figure S6 (Supporting Information) at positions approaching the negatively polarized electrode.

We show in the next how to use numerical simulations to extract ionic-related parameters through the analysis of currents in the zero-bias regime. As an example of the procedure, **Figure 2a** compares the recovery signal in the case of a microcrystalline
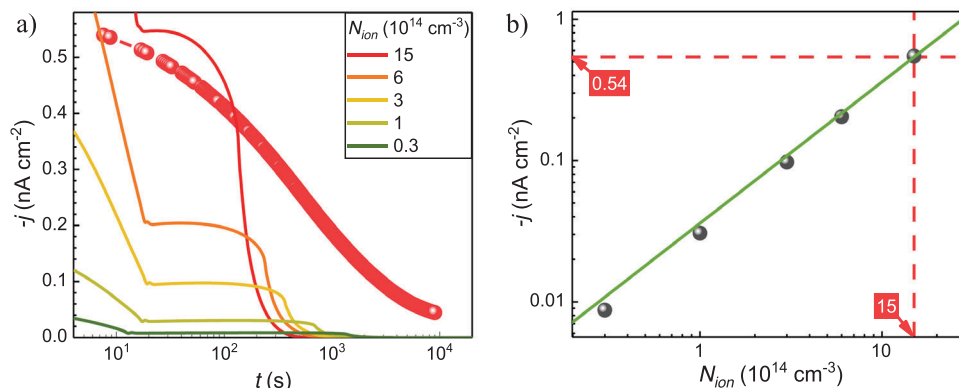
Figure 2. a) Example of the experimental current decay (dots) at $V = 0$ V after the previous 10 V polarization for ≈ 1.0 mm-thick MAPbBr$_3$-microcrystalline sample. Results of the 1D simulation (solid lines) for different ion concentrations. Ion mobility used in the simulation was $\mu_{ion} = 3 \times 10^{-7}$ cm^2 V^{-1} s^{-1}. b) Dark current plateau values at $t \approx 10$ s as a function of the ion concentration, indicating the extracted ion concentration value for the experimental current level.

MAPbBr$_3$ detector previously polarized at 10 V (dots), and the 1D numerical simulation results for different mobile ion concentrations (solid lines). Here ion mobility and the rest of the electronic (electrons and holes) parameters are kept as constants (see used values in Table S2, Supporting Information). By examining Figure 2a, one readily observes that the dark current smoothly decays in the experiment, while the simulation exhibits a more featured shape that signals a two-step depolarization process. At shorter times ($t < 10$ s), a sharp decrease appears that gives rise to a current plateau. Finally, the dark current rapidly vanishes with a characteristic time $\tau_{01} > 100$ s that depends on the ion concentration, in good accordance with Equation (2). Note that for a classical time-of-flight experiment ($\tau = L^2/\mu_{ion}V$) governed by the electric field $\xi = V/L$, the response time τ is independent on the ion concentration in opposition to the simulation curves. This fact reinforces our previous assumption in Equation (2).

It is nevertheless evident that the numerical simulation is not able to capture the experimental shape in Figure 2a. To rationalize this dissimilar behavior, we recall that our experimental set-up is limited by a sampling time of ≈ 10 s, which makes the initial rapid decay given by the simulation not accessible by the experiment. On the other hand, the sharp decay observed in the simulations at 10^2–10^3 s (depending on the ionic concentration) largely differs from the smoothy decrease exhibited by the experiment. We note here that the simulations perform a 1D numerical approach, unable to include further contributions to the relaxation time τ_{01} presumably resulting from the 3D inhomogeneity of the sample. Particularly, either structurally originated variations in μ_{ion} or local changes in the longitudinal path for the ionic migration have been observed between surface and crystal bulk transport,[32] which may be amplified in microcrystalline samples due to grain boundary effects. Because of the expected dispersion in τ_{01}, it is clear then that our numerical method only allows for parameter estimation, instead of curve fittings. Despite those limitations, the simulations can predict approximate values for the ion concentration (from the current plateau level at $t \approx 10$ s) and the characteristic decay time. As observed, the ion concentration value equals $N_{ion} = (1.5 \pm 0.1) \times 10^{15}$ cm^{-3} in good agreement with previously reported values. Here, the ion mobility used in the simulation was $\mu_{ion} = 3 \times 10^{-7}$ cm^2 V^{-1} s^{-1}. Corre-

spondingly, the simulated τ_{01} value is assumed to situate at times corresponding to half decay of the experimental curve, i.e., τ_{50}, capturing the expected dispersion in the decay time. Figure 2b shows the current plateau extracted at $t \approx 10$ s given by the simulation as a function of N_{ion}. As noted, both parameters exhibit a linear relation also in good accordance with Equation (1). An additional example, comparing another experimental measurement with simulations is shown in Figure S7 (Supporting Information).

As already mentioned, a fundamental mechanism for the device operation is the formation of ion space-charge zones near the contacts that eventually shrink when bias is removed at $V = 0$ V through a long depolarization process. Our 1D numerical simulation permits monitoring ionic space-charge profiles and their time evolution (originating the recovery dark current). An example of the time evolution in ion distribution with $N_{ion} = 10^{14}$ cm^{-3} and a sample thickness of 2 mm is shown in **Figure 3**. Note that our approach only uses cations as mobile ionic species (corresponding to bromide vacancies V_{Br}^+), which is considered to be kinetically active within the timescale of the experiment $t < 10^4$ s. Slower defects are discarded. As observed (Figure 3a), most of the sample bulk maintains the initial equilibrium concentration (and consequently a constant electrical field, as reported in Figure S8, Supporting Information), while ionic imbalance zones are formed in the vicinity of the outer electrodes. A close look at the contacts allows us to discern between two different ionic space-charge structures. A very narrow zone of nanometric width (related to L_D) develops at the negative electrode (Figure 3c) exhibiting a rather exponential ion accumulation, with ion concentration several orders of magnitude superior to the equilibrium value. The opposite positive electrode exhibits a dissimilar structure: an ion depletion is developed over an extended width, initially of the order of 20 μm, that eventually reduces with time as ions rearrange (Figure 3b). The depletion layer width within the perovskite can be written as[33–34]

$$w_d = \sqrt{\frac{2\varepsilon_0 \varepsilon_r}{q N_{ion}} V_{pre}} \qquad (3)$$
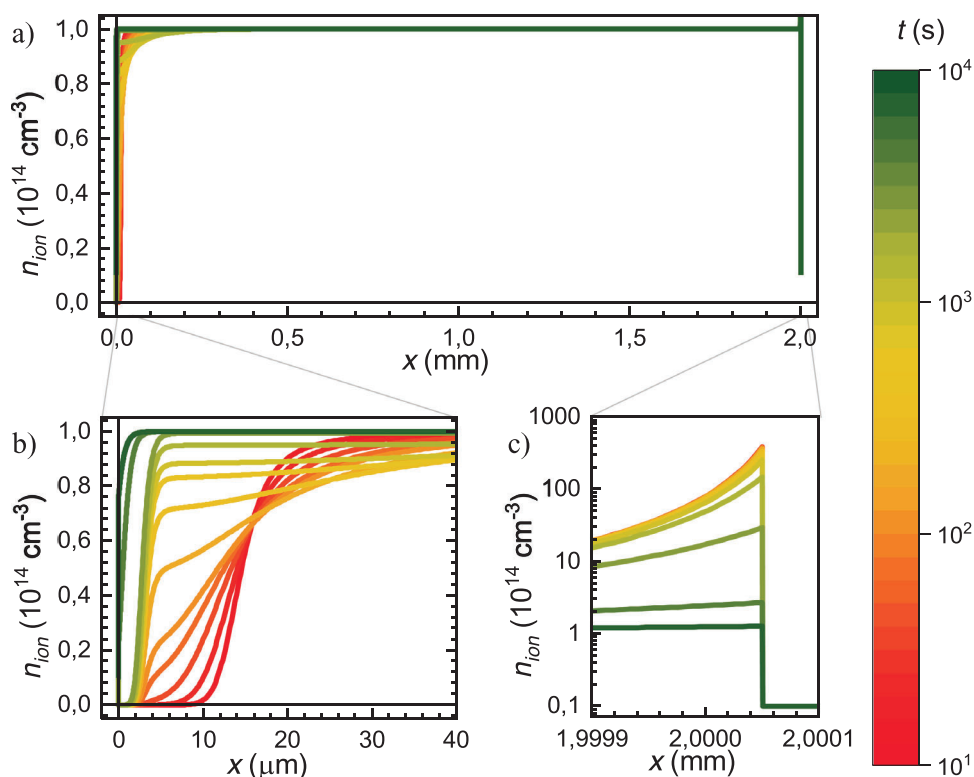
Figure 3. a) Spatially varying ion distribution n_{ion} at $V = 0$ V after previous 10 V polarization for 2.0 mm-thick sample with $N_{ion} = 10^{14}$ cm^{-3} and $\mu_{ion} = 10^{-7}$ cm^2 V^{-1} s^{-1}. Detail at b) positive and c) negative electrodes.

By evaluating Equation (3) with the used parameters in the simulation and $V_{pre} = 10$ V, The depletion layer width results in $w_d = 15$ μm. In previous publications,[12] the depletion layer width was parameterized in terms of the ion Debye length L_D as $w_d = \beta L_D$. Equation (3) allows to interpret the dimensionless parameter $\beta = (2qV_{pre}/k_BT)^{1/2}$, which in our analysis results in $\beta = 28$ for the used simulation inputs. It is also noted that the ion refilling of the space-charge depletion structure at the positive electrode follows a two-step mechanism: for $t < 5 \times 10^3$ s the depletion zone slowly collapses but leaving an empty layer of ≈ 2 μm in the vicinity of the contact, which finally disappears at longer times when the current rapidly vanishes. The distribution of electrical field, potential, and electronic carriers is shown in Figures S8–S11 (Supporting Information).

3. Conclusion

In summary, a connection has been established between the depolarization dark current and the mobile ion rearrangement after bias removal in single-crystal and microcrystalline millimeter-thick methylammonium-lead bromide samples. The analysis compares long-term dark current decays with the results of 1D numerical simulations. Both experiment and simulation exhibit long-term dark current decay signals as long as $t \approx 10^4$ s. The numerical simulation analysis predicts the formation of ionic space-charge zones in the vicinity of the outer contacts upon poling, while the perovskite layer maintains flat ion concentration profiles in the bulk. It is demonstrated that long-term current decay ($t > 10$ s) occurs by ion migration through charge drift (in most

of the sample bulk), while high-concentration gradients predict the occurrence of dominant diffusion currents (near the accumulation zones in the vicinity of the negative electrode). Assuming cations as mobile ionic species (corresponding to bromide vacancies V_{Br}^+), a depletion zone is developed near the positive contact with a width initially of the order of 20 μm. A narrower ion accumulation zone is built close to the negative electrode. Both space-charge zones collapse after bias removal following an initial ohmic ion drift mechanism that eventually evolves to diffusion-driven migration for longer times. Although simulations exhibit a more featured depolarization process, precluding consequently a true signal fitting, our approach can extract ion concentration values that approximate $N_{ion} \approx 10^{15}$ cm^{-3} in good agreement with previously reported values. Also, ion mobility is derived from the simulation in the range of $\mu_{ion} \approx 10^{-7}$ cm^2 V^{-1} s^{-1}. Relevant parameters for the assessment of X-ray detectors and other perovskite-based devices are then accessible by a simple measurement of dark current transients.

4. Experimental Section

Sample Characterization: In total, five samples were made for this study: two single crystals and three microcrystalline films. The fabrication procedure followed the steps described in the previous work,[6,35] and a summary of the samples properties is presented in Table S1 and Section S1 (Supporting Information). Optical transmission spectroscopy and powder X-ray diffraction patterns are presented in Figure S1 (Supporting Information). The optical bandgap, extracted from Tauc plot, shows a value of 2.21 eV and the diffractogram reveals the standard cubic space group

**ADVANCED
SCIENCE NEWS**

www.advancedsciencenews.com

**ADVANCED
ELECTRONIC
MATERIALS**
Open Access

www.advelectronicmat.de

Pm3m of MAPbBr$_3$ crystals with lattice dimension $a = 5.928$ Å, and without any trace of secondary phase. An optical profilometer (Bruker GT Contour) was used to estimate the surface roughness of the top and bottom surfaces. Figure S2 (Supporting Information) shows a smooth and shiny surface for the e- and some deep holes on the top surface of the microcrystalline samples. All the samples were polished prior to chromium electrode evaporation to make devices. In the symmetrically contacted samples, the top electrode (the one that receives the X-ray flux) was thinner (30 nm) than the bottom one (100 nm).

Electrical Measurements: The measurement of current-voltage-time characteristics was made with a Keithley 2636B SourceMeter. By examining Figure S3a (Supporting Information), one can infer that the current-voltage characteristics exhibit an approximate ohmic response within the selected voltage range, while small hysteretic effects were observed, for both symmetrically contacted - and microcrystalline perovskite samples. The *J–t* measurements were carried on with a Keithley 428 current amplifier and a Keithley 487 power supply limited by a sampling time of ≈ 10 s because of the registered decays as long as 10^4 s. The impedance measurements were carried out at room temperature, in the dark and air ambient conditions by using a PGSTAT-30 Autolab potentiostat equipped with an impedance module. From the impedance (Figure S3b, Supporting Information) and capacitance (Figure S3c, Supporting Information) responses, registered at zero-bias, two main features were observed: at high- and intermediate-frequencies ($f > 100$ Hz) the geometrical capacitance C_g is extracted from the plateau in Figure S3c (Supporting Information). Sample resistance R, determined from the intercept on the *x*-axis (Figure S3b, Supporting Information), is related to the sample conductivity σ as $R = \sigma L/A$, where A is electrode area and L sample thickness. It is known that $C_g = \epsilon_r \epsilon_0 A/L$ allows to estimate the dielectric constant $\epsilon_r < 100$ at 300 K, which agrees with previous determinations for MAPbBr$_3$, which resulted in values $\epsilon_r \approx 76$ at 300 K.[16,36] At lower-frequencies ($f < 10$ Hz) additional features were encountered in relation to interfacial mechanisms. These were modeled by means of the parallel combination $R_{LF}C_s$ accounting for the electronic/ionic charge accumulation in the vicinity of the contacts. The full spectra were analyzed and fitted in terms of the equivalent circuit given Figure S4 (Supporting Information).

Simulation Methods: The simulations were made within the framework of Driftfusion,[14] as a direct continuation of the previous work on the long-term polarization regimes of thick perovskite X-ray detectors,[12] ncluding both radiative and non-radiative recombination, and taking four main assumptions. First, (*I*) the bulk of the perovskite was initially taken as intrinsic, meaning that the total equilibrium concentrations of fixed and mobile ions should be balanced, i.e., the same total number of cations and anions (the simulation case), or effectively in the order of the intrinsic concentration (possible experimental situation). Second, (*II*) the interface regions between the perovskite and the contacts were unintendedly doped, forming depletion layers with thicknesses in the order of tens of nanometers. Third, (*III*) for the analyzed time-window only one type of mobile ions was considered to effectively contribute to the current and the reordering of the charge density profile. Lastly, (*IV*) the built-in field forming the Schottky-diode-like detector was only defined by the difference in work-function between the two metals, which was discarded in a symmetrical configuration. An illustrative set of simulation parameters is presented in Table S2 (Supporting Information) and a comprehensive explanation of the use and setting up of the Driftfusion code can be found in the original publication.[14]

Supporting Information

Supporting Information is available from the Wiley Online Library or from the author.

Acknowledgements

Conflict of Interest

The authors declare no conflict of interest.

Data Availability Statement

The data that support the findings of this study are available from the corresponding author upon reasonable request.

Keywords

[1] H. Wei, Y. Fang, P. Mulligan, W. Chuirazzi, H.-H. Fang, C. Wang, B. R. Ecker, Y. Gao, M. A. Loi, L. Cao, J. Huang, *Nat. Photonics* **2016**, *10*, 333.

[2] S. Deumel, A. van Breemen, G. Gelinck, B. Peeters, J. Maas, R. Verbeek, S. Shanmugam, H. Akkerman, E. Meulenkamp, J. E. Huerdler, M. Acharya, M. García-Batlle, O. Almora, A. Guerrero, G. Garcia-Belmonte, W. Heiss, O. Schmidt, S. F. Tedde, *Nat. Electron.* **2021**, *4*, 681.

[3] S. You, Z.-K. Zhu, S. Dai, J. Wu, Q. Guan, T. Zhu, P. Yu, C. Chen, Q. Chen, J. Luo, *Adv. Funct. Mater.* **2023**, *33*, 2303523.

[4] F. Liu, R. Wu, J. Wei, W. Nie, A. D. Mohite, S. Brovelli, L. Manna, H. Li, *ACS Energy Lett.* **2022**, *7*, 1066.

[5] Y. Liu, Z. Xu, Z. Yang, Y. Zhang, J. Cui, Y. He, H. Ye, K. Zhao, H. Sun, R. Lu, M. Liu, M. G. Kanatzidis, S. Liu, *Matter.* **2020**, *3*, 180.

[6] M. García-Batlle, J. Mayén Guillén, M. Chapran, O. Baussens, J. Zaccaro, J.-M. Verilhac, E. Gros-Daillon, A. Guerrero, O. Almora, G. Garcia-Belmonte, *ACS Energy Lett.* **2022**, *7*, 946.

[7] Y. Wu, J. Feng, Z. Yang, Y. Liu, S. Liu, *Adv. Sci.* **2023**, *10*, 2205536.

[8] L. Pan, S. Shrestha, N. Taylor, W. Nie, L. R. Cao, *Nat. Commun.* **2021**, *12*, 5258.

[9] M. García-Batlle, S. Deumel, J. E. Huerdler, S. F. Tedde, O. Almora, G. Garcia-Belmonte, *Adv. Photonics Res.* **2022**, *3*, 2200136.

[10] P. Jin, Y. Tang, D. Li, Y. Wang, P. Ran, C. Zhou, Y. Yuan, W. Zhu, T. Liu, K. Liang, C. Kuang, X. Liu, B. Zhu, Y. Yang, *Nat. Commun.* **2023**, *14*, 626.

[11] X. Xu, W. Qian, S. Xiao, J. Wang, S. Zheng, S. Yang, *EcoMat* **2020**, *2*, e12064.

[12] O. Almora, D. Miravet, I. Gelmetti, G. Garcia-Belmonte, *Phys. Status Solidi RRL* **2022**, *16*, 202200336.

[13] G. Armaroli, L. Maserati, A. Ciavatti, P. Vecchi, A. Piccioni, M. Foschi, V. Van der Meer, C. Cortese, M. Feldman, V. Foderà, T. Lemercier, J. Zaccaro, J. M. Guillén, E. Gros-Daillon, D. Fraboni, B. Cavalcoli, *ACS Energy Lett.* **2023**, *8*, 4371.

[14] P. Calado, I. Gelmetti, B. Hilton, M. Azzouzi, J. Nelson, P. R. F. Barnes, *J. Comput. Electron.* **2022**, *21*, 960.

[15] L. McGovern, M. H. Futscher, L. A. Muscarella, B. Ehrler, *J. Phys. Chem. Lett.* **2020**, *11*, 7127.

[16] M. García-Batlle, O. Baussens, S. Amari, J. Zaccaro, E. Gros-Daillon, J.-M. Verilhac, A. Guerrero, G. Garcia-Belmonte, *Adv. Electron. Mater.* **2020**, *6*, 2000485.

[17] M. García-Batlle, S. Deumel, J. E. Huerdler, S. F. Tedde, A. Guerrero, O. Almora, G. Garcia-Belmonte, *ACS Appl. Mater. Interfaces* **2021**, *13*, 35617.

[18] T.-Y. Yang, G. Gregori, N. Pellet, M. Grätzel, J. Maier, *Angew. Chem., Int. Ed.* **2015**, *54*, 7905.

[19] S. A. L. Weber, I. M. Hermes, S.-H. Turren-Cruz, C. Gort, V. W. Bergmann, L. Gilson, A. Hagfeldt, M. Graetzel, W. Tress, R. Berger, *Energy Environ. Sci.* **2018**, *11*, 2404.

[20] T. J. A. M. Smolders, A. B. Walker, M. J. Wolf, *J. Phys. Chem. Lett.* **2021**, *12*, 5169.

[21] T. J. A. M. Smolders, R. A. De Souza, A. B. Walker, M. J. Wolf, *Chem. Mater.* **2024**, *36*, 2334.

[22] L. Bertoluzzi, C. C. Boyd, N. Rolston, J. Xu, R. Prasanna, B. C. O'Regan, M. D. McGehee, *Joule* **2020**, *4*, 109.

[23] L. Bertoluzzi, J. B. Patel, K. A. Bush, C. C. Boyd, R. A. Kerner, B. C. O'Regan, M. D. McGehee, *Adv. Energy Mater.* **2021**, *11*, 2002614.

[24] B. Olyaeefar, S. Ahmadi-Kandjani, A. Asgari, *Phys. E* **2017**, *94*, 118.

[25] D. Moia, I. Gelmetti, P. Calado, Y. Hu, X. Li, P. Docampo, J. de Mello, J. Maier, J. Nelson, P. R. F. Barnes, *Phys. Rev. Appl.* **2022**, *18*, 044056.

[26] S. Jia, Y. Xiao, M. Hu, X. He, N. Bu, N. Li, Y. Liu, Y. Zhang, J. Cui, X. Ren, K. Zhao, M. Liu, S. Wang, N. Yuan, J. Ding, Z. Yang, S. Liu, *Adv. Mater. Technol.* **2022**, *7*, 2100908.

[27] A. O. Alvarez, F. Lédée, M. García-Batlle, P. López-Varo, E. Gros-Daillon, J. M. Guillén, J.-M. Verilhac, T. Lemercier, J. Zaccaro, L. F. Marsal, G. Garcia-Belmonte, O. Almora, *ACS Phys. Chem. Au* **2023**, *3*, 386.

[28] F. Lédée, J. Mayén-Guillen, S. Lombard, J. Zacarro, J.-M. Verilhac, E. Gros-Daillon, *J. Appl. Phys.* **2023**, *134*, 195703.

[29] H. Wang, Y. Bao, J. Li, D. Li, M. An, L. Tang, J. Li, H. Tang, Y. Chi, J. Xu, Y. Yang, *J. Phys. Chem. Lett.* **2023**, *14*, 9943.

[30] D. Moia, M. Jung, Y.-R. Wang, J. Maier, *Phys. Chem. Chem. Phys.* **2023**, *25*, 13335.

[31] M. Z. Bazant, K. Thornton, A. Ajdari, *Phys. Rev. E* **2004**, *70*, 021506.

[32] O. Almora, G. J. Matt, A. These, A. Kanak, I. Levchuk, S. Shrestha, A. Osvet, C. J. Brabec, G. Garcia-Belmonte, *J. Phys. Chem. Lett.* **2022**, *13*, 3824.

[33] M. H. Futscher, M. K. Gangishetty, D. N. Congreve, B. Ehrler, *J. Chem. Phys.* **2020**, *152*, 044202.

[34] O. Almora, C. Aranda, E. Mas-Marzá, G. Garcia-Belmonte, *Appl. Phys. Lett.* **2016**, *109*, 173903.

[35] O. Baussens, L. Maturana, S. Amari, J. Zaccaro, J.-M. Verilhac, L. Hirsch, E. Gros-Daillon, *Appl. Phys. Lett.* **2020**, *117*, 041904.

[36] S. Govinda, B. P. Kore, M. Bokdam, P. Mahale, A. Kumar, S. Pal, B. Bhattacharyya, J. Lahnsteiner, G. Kresse, C. Franchini, A. Pandey, D. D. Sarma, *J. Phys. Chem. Lett.* **2017**, *8*, 4113.